The Next Generation GPS Time

Ken L. Senior and Michael J. Coleman
U.S. Naval Research Laboratory Washington, DC 20375

Received April 2017; Revised July 2017

ABSTRACT: *The next generation Global Positioning System (GPS) ground control segment will entail a number of GPS ground system upgrades from the existing ground control segment. One of these upgrades is the inclusion of a new modernized timescale algorithm used to generate GPS Time. The timescale is currently being designed as a separate modular unit (given the acronym ETF, or Ensemble Timescale Filter) within the ground system navigation package and is based upon a U-D Kalman Filter implementation that utilizes measurements of all clocks in the ground network and satellite constellation.*

The new ETF module will include a number of features that improve the stability of the GPS Time timescale and provide more user/operator autonomy to include: multi-weight clock weighting for better handling of mixed clock types in the same filter; automated clock break detection and handling; robust outlier and anomalous clock behavior mitigation; admission of multiple external timescale solutions, including alternate ETF realizations; and adaptive clock parameter estimation. The preliminary results presented in this paper demonstrate some of the performance capabilities and robustness characteristics of the ETF. Published 2017. This article is a U.S. Government work and is in the public domain in the USA.

INTRODUCTION

The Global Positioning System (GPS) will be modernized within the decade in a number of different ways. Most notably, GPS III satellites are being designed and built in order to deliver greater accuracy and coverage for the entire GPS system and provide new modernized signals [1]. Along with upgrades to the space segment, the existing ground control segment is being modernized to enable command and control of the newer satellites and to provide improved accuracy of the GPS ephemeris/clock solutions and predictions through among other things improved satellite, clock, and geophysical modeling, and the incorporation of modernized GPS signals. The new upgraded ground control segment will consist of a complete modernization of all its elements, including but not limited to new modernized satellite tracking receivers, new ephemeris/clock estimation and control systems, and a new system for generating GPS system time, GPST [2]. In this paper, we will catalog some of the features that are anticipated to be part of the new timescale system and present some preliminary findings on its capabilities. Because this upgrade effort is ongoing, we note that any or all of the algorithm considerations presented here are subject to change based on future findings or determinations.

The module designed for integration with the GPS ground control segment is called the Ensemble Timescale Filter (ETF). This module is being customized to operate and interface with the orbit determination software being developed by the Jet Propulsion Lab (JPL), though it is an adaptation of many iterations of timescales developed at the Naval Research Laboratory (NRL) over the past decade. Earlier versions of this timescale have proven successful in a variety of implementations.

A predecessor of this timescale was implemented for the International GNSS Service (IGS) to provide a stable reference time for its clock solutions [3]. A second version was unveiled in 2011 that upgraded that timescale from a two-state model to a four-state one. The existing IGS timescale continues to benefit the Rapid and Final clock products in providing a stable reference.

At NRL, a similar version of this timescale has proven fruitful for two different applications. In the last decade, NRL researched the ability to synchronize and disseminate time between various ships and aircraft independent of GPS availability. This required a common time reference for which a timescale was utilized [4]. More recently, a laboratory time scale has been implemented to provide a robust time reference for life term GPS satellite clock testing [5].

Current efforts now focus on the development of the ETF module. This paper intends to communicate the scope of this module and document its

NAVIGATION: *Journal of The Institute of Navigation*
Vol. 64, No. 4, Winter 2017
Printed in the U.S.A.

fundamental models, routines, and analytical tools. Within this report, we also demonstrate its initial performance both in stability and prediction accuracy.

The models used in the ETF are presented in the first section. The base model is similar to the standard clock model of [6], which is sufficient for most of the ground station clocks. Additional states are added in order to handle periodics that are present in the data of satellite clocks. For this reason, expansions of the base model are presented. Further, a second expansion for an ensemble of clocks will also be presented as well as the approach for measurement updates.

In the following section, we catalog several functions that assist the Kalman Filter in identifying individual clock behavior. These monitors serve to diagnose clock data as either acceptable to or detrimental to the timescale. Protection of the clock ensemble is paramount and so these functions serve as an integral part of the stability of the ETF output.

The final section of this paper will show preliminary results for this timescale. The timescale is tested against GPS data from the National Geospatial- Intelligence Agency (NGA). The results section also includes an analysis of clock predictions based on the ETF's estimates of the clock states.

Notational Conventions

The following conventions have been selected and will be followed throughout this report. Clock difference measurements will be denoted by z_i^j which indicates a measurement of clock i with respect to clock j. Pseudo measurements (usually extrapolated from state predictions combined with measurements) will be denoted by $\tilde{z}_i^j$. In either case, a clock index of R will indicate a reference clock while e will indicate the ETF timescale itself. Some additional conventions are listed here:

- The independent epoch variable t has units of Modified Julian Date (MJD), unless otherwise noted.
- Vectors are denoted by lower case bold, such as $\mathbf{x}$.
- Matrices are denoted by upper case bold, such as $\mathbf{M}$.
- The italics form $M_{i,j}$ indicates the (i,j) entry of $\mathbf{M}$.
- To simplify notation in some instances, evaluation of a vector or matrix at a discrete epoch t_k can be denoted with a subscript as in $\mathbf{x}_k = \mathbf{x}(t_k)$.
- Minus sign superscripts (as in t_k^-) indicate *a priori* values of filter quantities. For example: $\hat{\mathbf{x}}_k^-$ indicates the state vector estimate propagated to t_k, but not yet updated in the Kalman Filter.
- The matrix $\mathbf{0}_n$ is the $n \times n$ zero matrix.
- The matrix $\mathbf{I}_n$ is the $n \times n$ identity matrix.

In the context of the GPS satellites, we also note that the term 'clock' here represents not only the physical oscillator, but also all delays in the dual frequency signal from the oscillator through the antenna. This is the only clock-like part of the signal observable with GPS measurements.

ENSEMBLE TIMESCALE FILTER

The primary purpose of the ensemble timescale filter is to filter noisy clock difference measurements that are formed (or measured) in the orbit determination process with respect to a chosen fixed reference clock in the network into estimates of the clocks re-aligned to a stable virtual reference timescale. The clock estimates from the orbit determination process are expressed with respect to the terrestrial time scale whose scale is consistent with UTC/TAI apart from a possible offset. These clock differences are therefore the inputs to the ETF. The core of the ETF is the Kalman Filter propagation and update procedures which predict and correct the model states as clock difference data are presented to the algorithm.

Base Clock Model

Estimates of a clock with a timescale ensemble as reference are attainable only if an accurate model of the clocks involved is applied. For the ETF, we consider a standard four-state clock model similar to the three-state model described in [6]. The continuous model which governs the dynamics of the state vector can be written in the form of the stochastic differential equation:

$$\begin{bmatrix} 0 & 0 & 0 & 0 \\ 0 & 1 & 0 & 0 \\ 0 & 0 & 1 & 0 \\ 0 & 0 & 0 & 1 \end{bmatrix} \frac{d\mathbf{x}}{dt} = \begin{bmatrix} 1 & -1 & 0 & 0 \\ 0 & 0 & 1 & 0 \\ 0 & 0 & 0 & 1 \\ 0 & 0 & 0 & 0 \end{bmatrix} \mathbf{x} + \mathbf{u}.$$

The components of the state vector $\mathbf{x}$ are:

$$\mathbf{x}(t) = \begin{bmatrix} \theta(t) & p(t) & f(t) & r(t) \end{bmatrix}^T,$$

where θ is the total phase offset (with respect to the timescale) of the clock including a white noise process; p is the phase offset of the clock without the additional white noise; f is the frequency offset of the clock; and, r is the drift offset.

There is also a corresponding white noise vector $\mathbf{u}$ which has these components:

$$\mathbf{u}(t) = \begin{bmatrix} u_\theta(t) & u_p(t) & u_f(t) & u_r(t) \end{bmatrix}^T,$$

where each element is a normally distributed random variable that simulates white noise. This noise,

added into the different states becomes: white noise in the phase (WNPH), random walk in the phase (RWPH), random walk in the frequency (RWFR), and random walk in the drift (RWDR), respectively.

This model differs from standard three-state models by the total phase state which contains an additional white noise process over the phase. Although this additional noise is indistinguishable from the measurement noise, it will be used to account for the relatively high phase noise in the Block IIR satellites. This total phase state will also be utilized to absorb the effects of all satellite clock harmonics as described below.

DISCRETE MODEL AND STATE PROPAGATION

The discretized model is obtained by integrating the continuous version via an inverse Laplace transform to obtain a state transition matrix Φ_B. The clock model then provides for the update of the clock states from one time epoch (t_{k-1}) to the next (t_k). We have,

$$\mathbf{x}_{k+1} = \Phi_B(\tau)\mathbf{x}_k + \int_{T_k} \Phi_B(\tau)\mathbf{u}\, dt, \tag{1}$$

where the time step is $\tau = t_k - t_{k-1}$, the interval of time $[t_{k-1}, t_k]$ is denoted by T_k and,

$$\Phi_B(\tau) = \begin{bmatrix} 0 & 1 & \tau & \tau^2/2 \\ 0 & 1 & \tau & \tau^2/2 \\ 0 & 0 & 1 & \tau \\ 0 & 0 & 0 & 1 \end{bmatrix}. \tag{2}$$

This base model alone is satisfactory for many of the ground stations in the NGA network. However, from some stations and all satellites, there are other systematic effects that require additional modeling as explained below.

Satellite Clock Model

The clocks aboard the GPS satellites exhibit periodics with periods of approximately 12 hours (once per revolution) and 6 hours (twice per revolution), as observed from any of the precision orbit and clock estimation products including those from the IGS and NGA. These appear roughly superimposed upon standard clock phase series. An exposition of these periodics and hypotheses regarding their origins is found in [7] and [8], respectively. We note from these references only the result that while some of the power at these periods may be owed to ephemeris error—and other known expected effects such as the relativistic 6-hour component owing to Earth's oblateness—most of the power at these periods cannot be attributed to these effects. Despite their source, these bias-like effects left untreated would impact any clock ensemble generated from the satellite clocks.

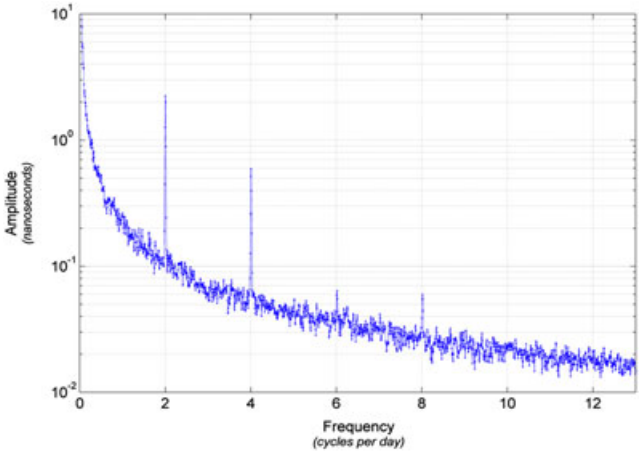

Fig. 1–Power spectral density of the Global Positioning System constellation clocks averaged (or stacked) in the frequency (Fourier) domain using International GNSS Service Final clock products over the period January through March 2015. [Color figure can be viewed at wileyonlinelibrary.com and www.ion.org]

Based on these analyses, additional optional states have been added to the NRL timescale filter in order to compensate for these effects [9]. Figure 1 shows the power spectral density of the GPS clocks averaged in the Fourier domain over the full constellation of clocks for the period January through March 2015 using IGS Final Clock Products (see http://www.igs.org/products). The magnitude of the harmonics across the constellation of clocks at frequencies of $2.003n$ cycles per day (cpd; $n = 1, 2, 3, 4$) is apparent. Given the strong energy at 2.003 and 4.006 cpd and the relatively weaker energy at other periods, we include enough states to model only two fixed-period harmonics. The ETF is configurable as to which periods are modeled, but is generally configured to model periods at $2.003n$ cpd with $n = 1, 2$ for the satellite clocks and set to 1 cpd for some stations exhibiting strong diurnal effects.

For a given clock i, a periodic at fixed frequency ν_i is modeled in the filter with two states a_i and b_i according to,

$$h_i(t) = a_i \cos(\nu_i t) + b_i \sin(\nu_i t).$$

While the frequency chosen is configurable in the filter, as mentioned above, the ones chosen generally for the satellites will be,

$$\nu_1 = 2\pi(2.003 \text{ cycles/day}),$$
$$\nu_2 = 2\pi(4.006 \text{ cycles/day}).$$

Given that one desires an estimation of the clock's phase, frequency, and drift offsets, we tie these harmonics to a 'total phase' state θ which is defined as

$$\theta(t) = p(t) + h_1(t) + h_2(t) + u_\theta(t). \tag{3}$$

The transition matrix used in the model of Equation (1) must be expanded from that matrix presented in Equation (2). The new transition matrix will take the form

$$\Phi_H(\tau) = \begin{bmatrix} \Phi_B & \mathbf{M}_k \\ \mathbf{0}_4 & \mathbf{I}_4 \end{bmatrix}, \tag{4}$$

where the upper right hand component correlates the harmonics into the total phase with the submatrix block

$$\mathbf{M}_k = \begin{bmatrix} \cos(\nu_1 t_k) & -\sin(\nu_1 t_k) & \cos(\nu_2 t_k) & -\sin(\nu_2 t_k) \\ 0 & 0 & 0 & 0 \\ 0 & 0 & 0 & 0 \\ 0 & 0 & 0 & 0 \end{bmatrix}.$$

This expanded transition matrix accompanies the expanded state vector given by

$$\mathbf{x}_k = \left[\theta(t_k) p(t_k) f(t_k)\, r(t_k)\, a_1(t_k)\, b_1(t_k)\, a_2(t_k)\, b_2(t_k)\right]^T.$$

Expansion for the Ensemble Model

Propagating the entire ensemble of clocks requires expanding the state and noise vectors even further to accommodate all clocks. The expanded vectors are formed by grouping the total phase states for all clocks at the top followed by the phase states for all clocks and then the frequency and drift states, and harmonic states if applicable.

$$\mathbf{x}(t) = \begin{bmatrix} \theta_1 \\ \theta_2 \\ \vdots \\ \theta_N \\ p_1 \\ p_2 \\ \vdots \\ p_N \\ f_1 \\ f_2 \\ \vdots \\ f_N \\ r_1 \\ r_2 \\ \vdots \\ r_N \end{bmatrix} \quad \text{and} \quad \mathbf{u}(t) = \begin{bmatrix} u_{\theta,1} \\ u_{\theta,2} \\ \vdots \\ u_{\theta,N} \\ u_{p,1} \\ u_{p,2} \\ \vdots \\ u_{p,N} \\ u_{f,1} \\ u_{f,2} \\ \vdots \\ u_{f,N} \\ u_{r,1} \\ u_{r,2} \\ \vdots \\ u_{r,N} \end{bmatrix}.$$

The transition matrix Φ is expanded by forming the product $\Phi = \Phi_H \otimes \mathbf{I}_N$, where $\otimes$ is the *Kronecker Product* [10]. The clock states and error covariances are thus propagated by:

$$\hat{\mathbf{x}}_k^- = \Phi \hat{\mathbf{x}}_{k-1} \qquad \mathbf{P}_k^- = \Phi \mathbf{P}_{k-1} \Phi^T + \mathbf{Q}_{k-1}. \tag{5}$$

The process noise matrix $\mathbf{Q}_k$ contributes additional noise to the covariance at each epoch. The level of this noise is directly dependent upon the matrix of spectral densities $\mathbf{S}$. For a single clock, this matrix is denoted by $\mathbf{S}$ and is equal to

$$E\left[\mathbf{u}\,\mathbf{u}^T\right] = \begin{bmatrix} S_\theta & & & & & & & \\ & S_p & & & & & & \\ & & S_f & & & & & \\ & & & S_r & & & & \\ & & & & S_1 & & & \\ & & & & & S_1 & & \\ & & & & & & S_2 & \\ & & & & & & & S_2 \end{bmatrix}. \tag{6}$$

Note that the four periodic states only have two spectral densities defined. Given the algebraic symmetry of these states' roles, it is sufficient that only one level of noise be defined for each periodic process. Hence, the continuous model for each periodic's states alone is (for $i = 1, 2$)

$$\begin{bmatrix} a_i \\ b_i \end{bmatrix}_{k+1} = \begin{bmatrix} a_i \\ b_i \end{bmatrix}_k + \int_{T_k} \begin{bmatrix} u_{a_i} \\ u_{b_i} \end{bmatrix} dt, \tag{7}$$

where $T_K = [t_{k-1}, t_k]$ and $u_{a_i} \sim u_{b_i} \sim \mathcal{N}(0, S_i)$.

For an ensemble of clocks, the matrix $\mathbf{S}$ is expanded to have size consistent with the matrices of Equation (5). See [11] and [12] for details on the development of this algorithm.

The actual implementation of the ETF utilizes a U-D square root decomposition of the covariance matrix in order to increase the dynamic range of the filter. This entails, specifically, processing two factors of the covariance: a diagonal matrix $\mathbf{D}$ and an upper triangular matrix $\mathbf{U}$. At any epoch, the total covariance matrix is realized by

$$\mathbf{P}_k = \mathbf{U}_k \mathbf{D}_k \mathbf{U}_k^T, \tag{8}$$

although this matrix product is computationally expensive and therefore performed infrequently.

Propagation and update algorithms by Thorton and Bierman are utilized to handle the Kalman Filter's processing of the $\mathbf{U}$ and $\mathbf{D}$ factors in an efficient manner. Details for these algorithms are documented in [13]. The authors have made some modifications to these algorithms specific to the ETF implementation. These changes have been largely to take advantage of sparsity of the covariance matrix in order to increase algorithm speed and also other changes tailored to the algorithm's specific needs.

KALMAN GAIN AND UPDATE

Following the propagation stage, the newly computed *a priori* states $\hat{\mathbf{x}}_k^-$ are compared to the data set $\{\mathbf{z}_k\}$ via the observation equation

$$\mathbf{z}_k = \mathbf{H}\hat{\mathbf{x}}_k^- + \varepsilon \tag{9}$$

where $\mathbf{H}$ is the observation matrix and ε is the measurement noise which has a corresponding covariance matrix

$$\mathbf{R} = E\left[\varepsilon\varepsilon^T\right].$$

The observation matrix is filled in a way that ties the measurements and states together in

$$z_i^R = \hat{\theta}_i^- - \hat{\theta}_R^- + \varepsilon_i^R, \tag{10}$$

where z_i^R is the measurement of clock i with respect to the reference clock R, ε_i^R is the noise associated with that measurement and $\hat{\theta}_i$ is the total phase estimate of the clock i with respect to the timescale ensemble. There are $N-1$ rows of $\mathbf{H}$ associated with Equation (10); one row for each clock $i \neq R$.

Having only $N-1$ clock difference measurements in order to estimate N individual sets of clock states represents a rank deficiency or observability problem in the estimation which will ultimately lead to filter divergence if not treated.

This observability problem is addressed by imposing the following set of timescale constraints:

$$\begin{aligned}
\sum_{i=1}^{N} w_i^{\theta}\left(\hat{\theta}_i(t+\delta \mid t) - \hat{\theta}_i(t+\delta)\right) &= 0,\\
\sum_{i=1}^{N} w_i^{p}\left(\hat{p}_i(t+\delta \mid t) - \hat{p}_i(t+\delta)\right) &= 0,\\
\sum_{i=1}^{N} w_i^{f}\left(\hat{f}_i(t+\delta \mid t) - \hat{f}_i(t+\delta)\right) &= 0,\\
\sum_{i=1}^{N} w_i^{r}\left(\hat{r}_i(t+\delta \mid t) - \hat{r}_i(t+\delta)\right) &= 0.
\end{aligned} \tag{11}$$

Note that there is one constraint for each noise class of the base clock model; additional constraints for the noises driving the harmonic states are not included since it is believed these effects are largely deterministic. So, four sets of associated clock weights, $\{w_i^{\theta}\}$, $\{w_i^{p}\}$, $\{w_i^{f}\}$, and $\{w_i^{r}\}$ are utilized to further constrain the estimation, where each set of weights is set inverse to the level of the respective noises and normalized to sum to one over the set of clocks contributing to the ensemble. For example, assuming the validity of the model, the actual estimated drift $\hat{r}_i(t+\delta)$ at $t+\delta$ will differ from its predicted value $\hat{r}_i(t+\delta \mid t)$ exactly by its random walk drift and so normalizing each clock's random walk drift contribution by setting w_i^r inverse to the level of its random walk drift will enforce the constraint that the normalized sum of the random walk drifts be zero over the ensemble; similar approaches are taken for the other noise processes. A full discussion on the use of multiple clock weights and its benefits are presented in [14].

One primary benefit of constraining the different classes of noises independently with separate timescale weighting constraints is that one may optimally combine differing classes of clocks together in a single filter. For example, active hydrogen masers typically demonstrate lower levels of RWPH noise as compared to cesiums standards. Hydrogen masers, however, exhibit higher levels of RWDR noise as compared to cesiums. By constraining these noise types independently the resulting timescale will combine the masers and cesiums to produce a timescale that is more stable than any of these constituent clocks. Figure 2 demonstrates the benefit of this form of weighting. The figure shows the stability results in the form of Hadamard deviation of a simulation of two classes of clocks, one class having lower levels of RWPH noise as compared to the other class, and one having lower levels of RWFR noise. The resulting multi-weighted timescale stability is better at all averaging intervals, effectively taking advantage of the stability of both classes of clocks.

The Kalman Gain at each epoch is written as,

$$\mathbf{K}_k = \mathbf{P}_k^- \mathbf{H}^T \left(\mathbf{H}\mathbf{P}_k^- \mathbf{H}^T + \mathbf{R}\right)^{-1}, \tag{12}$$

though the gain is not actually formed as a matrix inversion in the U-D mechanization but rather performed in a scalar operation (c.f., [13]).

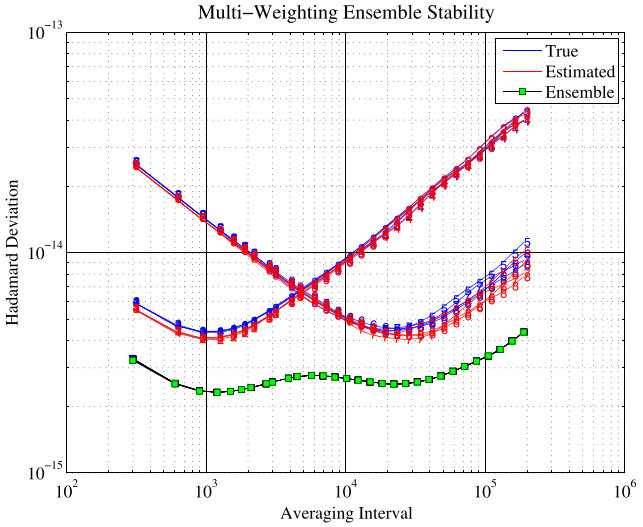

Fig. 2–Stability of a multi-weighted ensemble timescale from a simulation of two classes of clocks, one class having lower levels of random walk in the phase noise but higher levels of random walk in the frequency noise, and the other class having correspondingly higher levels of random walk in the phase noise but lower levels of random walk in the frequency noise. Multiple clock weighting produces a timescale (green curve) that is more stable at all averaging intervals. Note that the simulation and resulting stability is unitless; the results of the ensemble combination are invariant to the particular unit or scale. [Color figure can be viewed at wileyonlinelibrary.com and www.ion.org]

Finally, the *a priori* states $\mathbf{x}^-$ are updated to *a posteriori* states using the update equations

$$\hat{\mathbf{x}}_k = \hat{\mathbf{x}}_k^- + \mathbf{K}\left(\mathbf{z}_k - \mathbf{H}\,\hat{\mathbf{x}}_k^-\right) \quad \text{and} \quad \mathbf{P}_k = \mathbf{P}_k^- - \mathbf{KHP}_k^-. \tag{13}$$

Note that filtering the set of $N-1$ clock difference measurements in Equation (10) along with the additional timescale constraints of Equation (11) solves the observability estimation problem. Hence, we are able to produce N individual sets of clock states and covariances relative to the ensemble timescale as shown in Equation (13).

See [11] or [12] for details on the development of the continuous and/or discrete time model.

AUXILIARY FUNCTIONS

In the following sections, we describe additional ETF algorithm functions that are included to deal with several practical problems often encountered in filtering clock data, including mitigation of bad measurements, mitigation of discrete changes in a clock's state(s), and adaptive estimation of poorly known clock parameter values, or clock noise densities.

Pivot Clock Selection

At any given epoch, the clock measurement process may produce faulty or bad measurements, or a clock may deviate from its prescribed model and parameters. As described below, prefit residuals of the clock data and states may be examined to detect such anomalous behavior. However, if the anomalous behavior occurs with the fixed reference clock that was chosen in the clock/orbit estimation process, then all clock measurements will exhibit the behavior making such detection difficult. To avoid this problem, a procedure is implemented to re-reference all clock measurements to a new reference clock (or *pivot clock*) that is determined to be operating nominally according to its model and whose measurement is determined as good; this pivot clock selection is made at every epoch and as such may change at every epoch. Notationally, we designate this pivot clock with index p.

This routine first forms the set of pairwise clock innovations (also called prefit residuals). These are calculated by

$$\gamma_i^r(t_k) = z_i^r(t_k) - \hat{\theta}_i(t_k^-) + \hat{\theta}_r(t_k^-), \tag{14}$$

where r is the index corresponding to the data set's reference clock. The pivot clock p is chosen such that

$$\mid \gamma_p^r - M \mid \;=\; \min_{1\le i\le N} \mid \gamma_i^r - M \mid,$$

where M is the maximum likelihood estimator of the set $\{\gamma_i^r\}_i$. This technique was first suggested by Percival in [15] and later cast into the Kalman Formalism by Stein in [16].

Clock Break Detection and Handling

Mitigating the effect of anomalous measurements on the timescale is critical for automatic long term operation. The ETF monitors the prefit residuals for each clock in order to detect any anomalous behavior and corrects for problems that typically occur, such as discrete changes (or breaks) in phase or frequency. The innovations are also used to gracefully down-weight any measurements that are only marginally bad, thereby promoting more gradual changes in the clock weights and improved timescale stability.

Measurement weights are established for every clock data point at every epoch. Using the propagated total phase states for both the clock i and pivot clock p, one can calculate pairwise innovation $\gamma_i^p(t_k)$ as defined in Equation (14). Note that these innovations are statistics of the distribution

$$\mathcal{N}\Big(0\,,\,P_{i,i} + P_{p,p} + R_{i,i}\Big),$$

where $P_{i,i}$ is the variance on the total phase estimate of clock i, $P_{p,p}$ is the variance on the total phase estimate of clock p, and $R_{i,i}$ is the variance of the measurement noise for clock i. In order that the innovations be consistent in scale from one clock to the next, we scale these to the standard normal Z statistic and calculate the number of sigma deviations from the expected zero mean. This number of standard deviations is

$$n_i^p(t_k) \;=\; \frac{\gamma_i^p(t_k)}{\sqrt{P_{i,i} + P_{p,p} + R_{i,i}}}. \tag{15}$$

As mentioned above, gradual measurement weighting is employed in the ETF. That is, the measurement weight for clock i carries a full weight of $\rho_i = 1$ in the Kalman update as long as the number of sigmas $n_i^p(t_k)$ from Equation (15) is limited to 3.5. For values of $n_i^p(t_k)$ beyond this, the measurement weight is reduced until reaching $\rho_i = 0$ at $n_i^p(t_k) = 5$. The Hampel Psi function is utilized to compute these tapered measurement weights, where the function is defined as

$$\Psi_{a,b}(x) = \begin{cases} x & \text{if } 0 \le |x| < a; \\ \frac{a}{a-b}(x - \text{sgn}(x)b) & \text{if } a \le |x| < b; \\ 0 & \text{if } b < |x| \end{cases}.$$

The number of sigmas bounding full weight versus unweighted (namely $a = 3.5$ and $b = 5.0$ from above) are configurable based on the flexibility needed by the user.

The clock break detection relies heavily on these measurement weights, ρ_i. The ETF tracks a brief history of each clock's measurement weights and decides under what condition the clock is operating. The detection of and compensation for any potential breaks follows a series of automated investigations each time a clock has a down-weighted measurement. Based on the history and current conditions, one of the following clock statuses is assigned.

- **Steady State**: Data for this clock is free of outliers and has not seen anomalies for some prescribed amount of time and variances have reached an asymptotic level.
- **Outlier**: Sudden data point that yields measurement weight of 0; clock remains an ensemble member.
- **Phase Break**: Consistent outliers for at least k_1 epochs in a row; clock may be removed from ensemble for short time.
- **Frequency Break**: At least k_2 phase breaks since last epoch where $\rho_i(t_k) \neq 0$; clock removed from ensemble and decorrelated from other clock states and noise is injected into the clock's frequency variance in order to adjust more quickly to any new frequency offset.
- **Clock Reset**: At least k_3 frequency breaks since last epoch where $\rho_i(t_k) \neq 0$; at this point, it is clear that auto correction cannot establish estimates consistent with data for the break observed; clock states and covariances are cleared and reinitialized.

The parameters $k_1, k_2,$ and k_3 are configurable based on the desired sensitivity of the auto breaking routine. Figure 3 demonstrates the reaction of the ETF auto-break detection and compensation routine as it detects and adjusts for three anomalous behaviors, outliers, a phase break, and a frequency break. In all cases the problem is detected, measurements are down-weighted, and the problem is corrected without any impact to the resulting ensemble.

Spectral Density Parameter Estimation

At each epoch's propagation stage, integrated process noise **Q** is added to the states' variances as presented in Equation (5). The level of variance increase (or noise injection) depends directly on the clock's process noise spectral densities **S**. These values are input parameters to the filter and determine

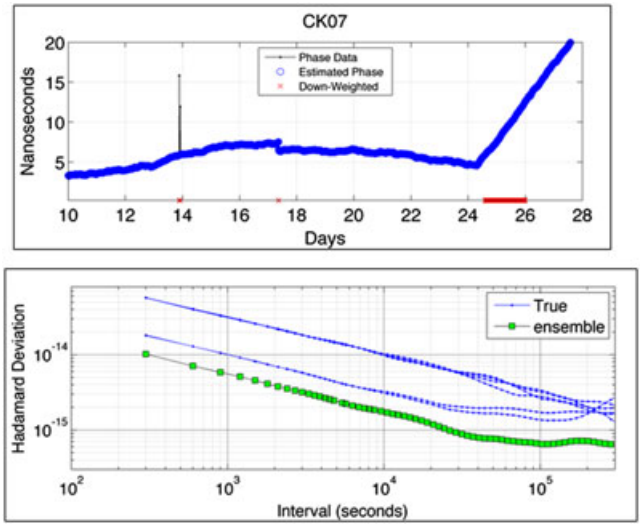

Fig. 3–Simulation example showing the automatic detection and adjustment by the Ensemble Timescale Filter of three kinds of anomalous clock behaviors, including measurement outliers, a phase break, and a frequency break. The top panel shows the phase offset of the clock and the bottom panel shows the clock stabilities and ensemble timescale stability as measured by the Hadamard deviation statistic. The red x markers in the top panel indicate the locations at which anomalous behavior was detected, measurements down-weighted, and each problem properly compensated. In all cases, the ensemble was protected from the anomalous behaviors. [Color figure can be viewed at wileyonlinelibrary.com and www.ion.org]

the tolerance level of the measurement to state offset. The dissociation of measurement noise to the various clock states is therefore dependent on these **Q** values.

It is important that a clock's spectral densities are not less than the typical level of noise in the actual clock measurement. In such a case, the residual noise will be allocated to another clock's state variance or the ensemble itself. If the densities are greater than the typical noise level, then large measurement anomalies or clock breaks will be accepted and absorbed by the Kalman Filter. For these reasons, the most accurate possible clock densities are desired.

The spectral densities, in Equation (6) may be determined for a clock by analyzing the Hadamard variance of its measured phase data. Since all such phase measurements have a common reference clock, an appropriate method to extract the correct density for each clock (and not the reference clock) is the N-cornered hat approach [17].

Computation of these densities can be made by comparing the Overlapped Hadamard Deviation at various averaging intervals and calculating densities respectively. Table 1 catalogs these relationships and a development of these relationships is found in [18].

Table 1 — Relationship of each Ensemble Timescale Filter noise density parameter and the Hadamard statistic $\sigma_H^2(\tau)$ for averaging intervals τ. Where necessary to ensure convergence of the spectral density, a Fourier high cutoff frequency f_h has been imposed

Noise Name	State Spectral Filter Density	Hadamard Variance	Units of State (base sec)
WNPH	S_θ	$3\tau^2\sigma_H^2(\tau)/(10f_h)$	s^2
RWPH	S_p	$\tau\sigma_H^2(\tau)$	s
RWFR	S_f	$6\sigma_H^2(\tau)/\tau$	s^{-1}
RWDR	S_r	$120\sigma_H^2(\tau)/(11\tau^3)$	s^{-3}

This process, however, assumes the availability of healthy clock data before the real-time use of the filter. Even if such data can be used, a clock's performance is bound to change over it's life time, and hence its noise profiles will follow suit. Therefore, the ETF also employs an optional adaptive clock parameter estimation procedure for automatically estimating clock densities corresponding to the densities of the base clock model. The procedure is not documented here but follows closely to the one described in [19].

Algorithm Summary

In addition to the usual Kalman Filter components, the timescale algorithm employed in this analysis entails several additional features. At each epoch of discrete data, the algorithm completes a single step that proceeds through the following.

- Receive this epoch's clock difference measurements.
- Choose a reliable pivot clock and re-reference measurements to it.
- Set observation matrices and calculate clock weights/constraints such that they satisfy Equation (11) and also distribute larger amounts of weight to clocks that are quieter in each respective noise class. Upper limits on clock weights are imposed to prevent timescale domination by any one clock. In the event the upper limit is reached, each weight larger than the upper limit is reduced by a small amount and weights are then re-normalized. The process is iteratively repeated until the upper limit condition holds true.
- Kalman Filter state propagation of Equation (5).
- Measurement weights. Based on Equation (9), the existing states are compared to observations and residuals can be determined. Clocks with substantial residuals will have their measurements reduced in weight.
- Kalman Filter state update of Equation (13).
- Post processing analysis: clock break detection, adaptive $\mathbf{Q}$ estimation, ensemble steering.
- Export clock state estimates and variances.

CALCULATIONS & ANALYSIS

This final section presents results from a test of the ETF on data from the NGA. Analysis of both the stability of the timescale as well as the clock predictions obtained from the computed clock state estimates will be shown.

Throughout this section, we will often employ a median computation MEST in place of a standard statistical median. The MEST computation is a maximum likelihood estimator that offers the benefit of averaging but also robustness against outliers. Its uses and applications in timescales have been documented by Don Percival in [15]. Matlab® source code for this algorithm is provided in the appendices below.

The total phase states of Equation (13) are the phase offsets of each clock relative to the ensemble. That is, the timescale is accessed (in time) by using these estimated time offsets of each clock relative to the timescale. A somewhat 'noisier' version of the time offset of the timescale relative to each clock can be defined by

$$\tilde{z}_e^R(t_k) \;:=\; \underset{1\le i\le N}{\text{mest}} \left\{ z_i^R(t_k) - \hat{\theta}_i^e(t_k) \right\}.$$

This quantity is a 'measured' representation of the original measurement system reference clock versus the timescale. Each clock may then be aligned to the ensemble by simple differences,

$$\tilde{z}_i^e \;=\; z_i^R - \tilde{z}_e^R. \tag{16}$$

One advantage of using Equation (16) over the clock's phase estimates relative to the ensemble, $\hat{\theta}_i$, is that clock differences are preserved. That is,

$$z_i^R - z_j^R \;=\; \tilde{z}_i^e - \tilde{z}_j^e$$

for all i and j. Therefore, re-aligning measurements to the ensemble in this way results in a collection of measurements for which the timescale realignment does not impact the navigation solution.

Another advantage of using the measured representation of each clock versus the timescale over the filter's phase estimates is that phase estimates may be over or under smoothed depending on the quality of the clock densities used. Also, if a clock has been reset, newly entered into the filter, or is otherwise undergoing any other filter function for which its states are still transitioning to steady state, then the

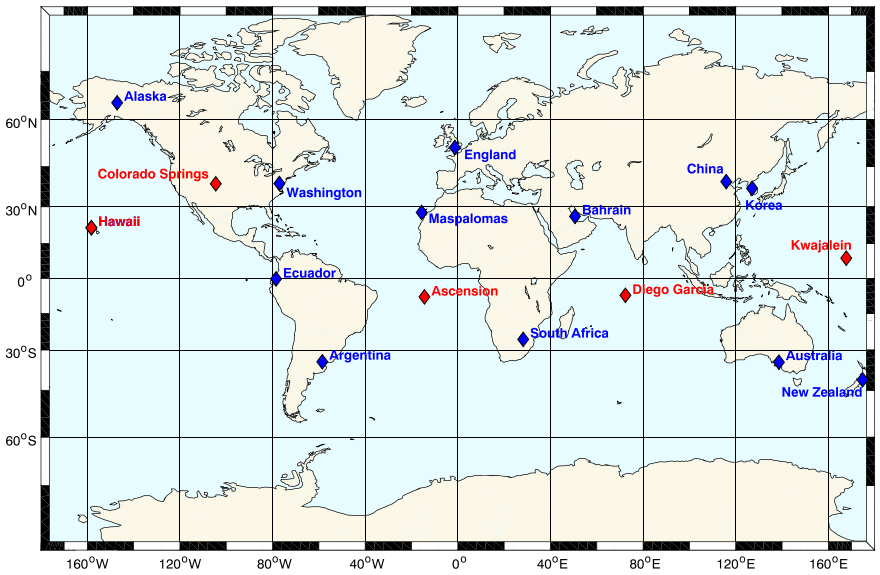

Fig. 4–Map shows the locations of Air Force (red) and National Geospatial-Intelligence Agency (blue) Global Positioning System tracking stations. [Color figure can be viewed at wileyonlinelibrary.com and www.ion.org]

filter's estimates are not yet reliable for that clock; the measured representation of that clock versus the ensemble will be reliable in all these cases.

For these reasons, all analysis below uses the measured representation of each clock relative to the ensemble.

NGA 112 Day Data Set

The test whose results are shown in this section utilizes NGA and Air Force tracking network RINEX data for the entire GPS constellation and associated ground network clocks. Thirty-second RINEX data were processed through the JPL OCX orbit and clock determination software, called 'RTGx' [20]. Clock estimates for the GPS satellite clocks and ground network clocks from RTGx were then processed through ETF for the results of this section. The specifics on the dataset:

- Start Date: MJD 57000 (2014 Dec 09)
- End Date: MJD 57112 (2015 Mar 31)
- Length of Test Run: 112 Days
- RINEX Data Interval: 30 seconds
- Clock Estimate Interval: 5 minutes
- Included 17 ground stations as shown in Figure 4.
- All satellite and ground clocks whose data were available were estimated in the ETF; however, anomalous clocks (see Figure 7 later in this paper) were not admitted as ensemble members (i.e., weights forced to zero); see Table 2 for the distribution of satellite clocks across the blocks.

These data were selected because the collection of clocks and location of tracking stations in the NGA/AF network closely resemble the network that will comprise the OCX network, including high performance commercial cesium clocks in the tracking stations and the UTC(USNO) master clock(s) in Washington, D.C. and Colorado. Nonetheless, it should be noted that the results herein will not be truly representative of the next generation ground control network since other improvements in satellite and geophysical modeling, receiver technology, and improved signals expected in the upgrade are not realized in these data.

The GPS satellite clocks that are active and whose data are utilized for this test depend very much on the range of dates selected. In fact, the choice of 57000–57112 was selected since there were minimal changes in the SVN/PRN assignments and no changes to the active clock on any of the satellites. The only exception is PRN26 which was undergoing a decommissioning beginning at 57027. A summary of the satellite distribution by block and active clock type are outlined in Table 2.

During the period of data selected, there were a number of known events in the GPS Constellation initiated by the GPS control segment, including

Table 2—Satellite Clock Types active during the data set period of 57000–57112.

Block	Active Clock	Number of Satellites
Block IIA	Cesium	3
	Rubidium	2
Block IIR	Rubidium	12
Block IIR-M	Rubidium	7
Block IIF	Cesium	1
	Rubidium	7

Table 3 — GPS Master Control Events. These events are those that occurred for the satellites between the dates of 2014 Dec 09 an 2015 Mar 31. PRN codes skipped in this table do not have officially documented events in the NRL GPS Quarterly Reports; see [21] and [22]. Comments in red are not in the reports, but rather observations noted by the authors.

PRN	SVN	DATE	EVENTS / COMMENTS
03	69	Dec 12	Set unusable.
		Mar 02	Unknown frequency break.
05	50	Jan 23	Clock drift upload.
06	67	Jan 28	Clock drift upload.
07	48	Dec 19	SVN maneuver.
08	38	Jan 03	Returned to operations; transmitted as PRN08; remained unusable.
		Jan 29	SVN maneuver.
09	68	Jan 28	Clock drift upload.
11	46	Excessive frequency/drift breaking.	
13	43	Jan 09	SVN maneuver.
15	55	Dec 11	SVN maneuver.
17	53	Jan 22	Unknown frequency break.
		Excessive frequency breaking.	
20	51	Dec 16	SVN maneuver.
21	45	Jan 18	Unknown frequency break.
		Jan 20	Unknown frequency breaks.
		Jan 23	Clock drift upload.
22	47	Excessive frequency breaking.	
26	26	Jan 05	Set unusable.
		Jan 06	Decommissioned from PRN.
	32	Feb 05	Returned to operations; transmitted as PRN 26; remained unusable.
		Feb 24	Returned to disposal operations.
	27	Feb 26	Returned to operations; transmitted as PRN 26; remained unusable.
		Mar 16	Returned to disposal operations.
28	44	Unmodeled and unexplained harmonics having approximately 15 ns amplitude and 5 day period.	
29	57	Excessive frequency breaking.	
30	64	Jan 24	Ephemeris issue.
32	23	Mar 20	SVN maneuver.

Delta-V maneuvers and satellite clock drift uploads. Some events are caused by unknown sources; see Table 3 for details. For known events, manual frequency or drift changes were ingested into the ETF at the appropriate epoch to account for the effects on frequency or drift in the same way that operations might schedule such events in advance, or rewind the filter to incorporate the changes manually. For unknown events, such as spontaneous random frequency jumps in the rubidium clocks, the ETF was left to deal with these using the auto-break adjustment mechanism.

Table 3 also shows some comments made by the authors (printed in red) after a post-processed analysis was made. Although events are tracked for the GPS Quarterly Reports, not every characteristic that can cause poor predictions is accounted for. Large numbers of frequency breaks, or phase data that are uncharacteristic of the clock model are only two examples of problematic clock behavior. These considerations must be made when analyzing the prediction results.

ETF Stability Test

The NGA/AF test RINEX data set was processed through the JPL RTGx software, and subsequent clock estimates were then processed through the ETF. All resulting clock estimates within the ETF were aligned to the timescale using the measured timescale representation described above, i.e.,

$$\tilde{z}_i^e = z_i^R - \tilde{z}_e^R, \tag{17}$$

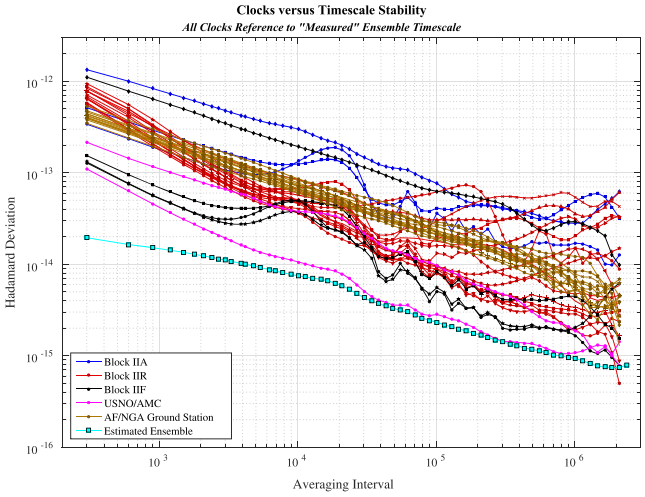

Fig. 5–Frequency stability of the GPS constellation of clocks as measured by the Hadamard deviation statistic relative to the ETF ensemble as well as estimates of the stability of the ETF ensemble itself from processing of the NGA dataset. The test results shown are for the period 1 January 2015 through 31 March 2015. [Color figure can be viewed at wileyonlinelibrary.com and www.ion.org]

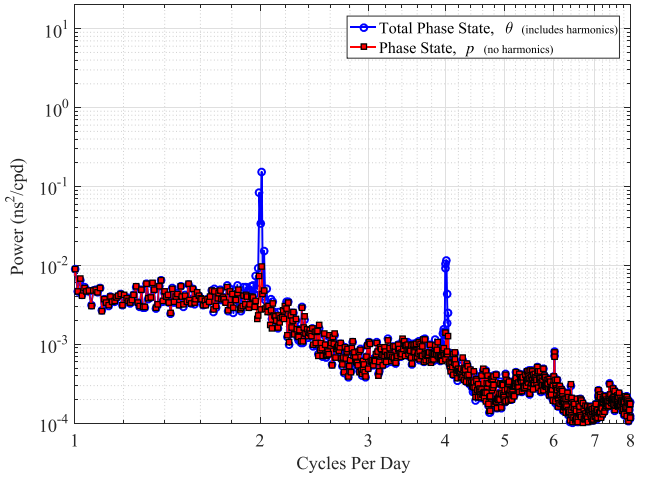

Fig. 6–Power Spectral Density of the phase and total phase states for all satellite clocks stacked in the Fourier domain for the full constellation; note that a Blackmanharris window was used in the calculation of the PSD. [Color figure can be viewed at wileyonlinelibrary.com and www.ion.org]

where R is the reference clock of the input measurements. Summary statistics of each of these measured series were calculated using the Hadamard deviation statistic applied over the period 1 January through 31 March 2015; data for the first twenty days of the test in December 2014 were ignored for purposes of analyzing timescale stability to provide sufficient time for clocks to reach steady state in the filter. Figure 5 shows the resulting statistics with each satellite clock colored by satellite block.

A statistical estimate of the timescale stability (shown in green) was also calculated using

$$H\sigma_e^2(\tau) = \sum_{i=1}^{N} w_i^2 \, H\sigma_i^2(\tau), \qquad (18)$$

where w_i is the average weight of the clock i over the test period and $H\sigma_i$ is the Hadamard deviation of the series calculated in Equation (17) for clock i. It is noted that during the test period, the average clock weights were, $3.8\%, 3.8\%, 3.6\%, and\ 3.8\%$, respectively, for each of the four clock weights of Equation (11) and the maximum weight was 9.0% for all four weights held by the clock at USNO. Based on the maximum weights and the banding of the Hadamard series in Figure 5, we believe the estimate shown is a good estimate of the timescale stability. The resulting timescale stability is better than any member clock at all averaging intervals and achieves very good stability, showing in the upper 10^{-16} level for $\tau > 12$ days.

Satellite Clock Harmonics

As detailed earlier in this paper, the satellite clocks exhibit periodics in their data and four states of our clock model are allocated to estimate them.

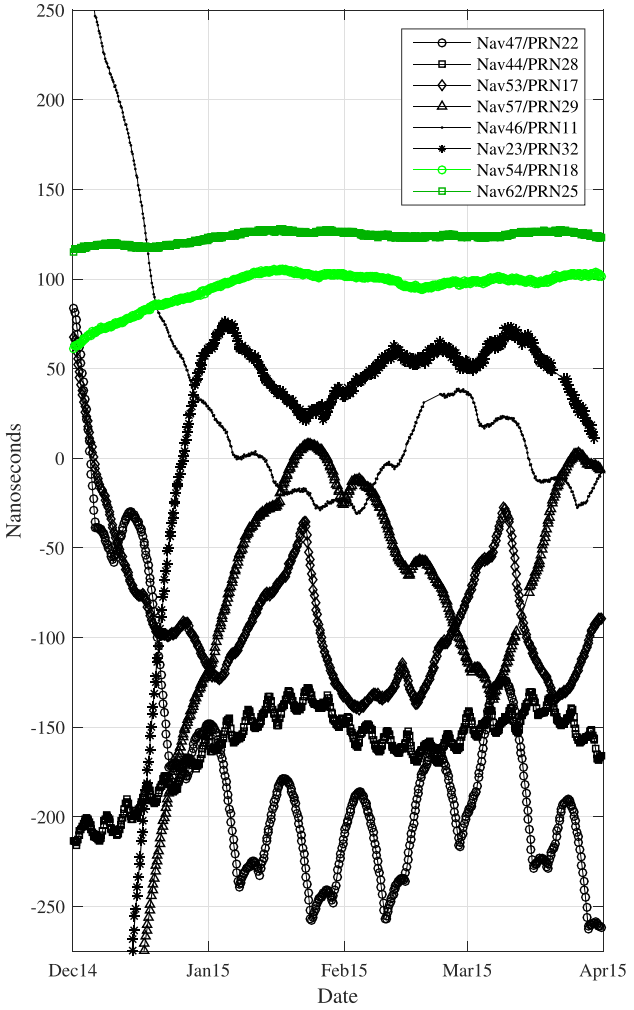

Fig. 7–Phase offset of several clocks with respect to the measured ensemble. This figure demonstrates several anomalous clocks (shown in black series) not performing according to the ETF model; for comparison, two well-performing clocks are shown in green. [Color figure can be viewed at wileyonlinelibrary.com and www.ion.org]

The power spectral density plot in Figure 6 depicts the results of filtering the NGA test data set with the new harmonic states enabled for periods 2.003 and 4.006 cpd. The power spectral density is computed for both the total phase estimate series, $\hat{\theta}_i(t)$, and the phase estimate series, $\hat{p}_i(t)$, and again stacked (averaged) together in the Fourier domain across the full constellation.

Note that the blue line showing the PSD of the constellation total phase states recovers the same amplitude energy shown earlier in Figure 1 at the periodic frequency of 2.003 and a smaller fraction of the energy for 4.006 cpd. By contrast, almost no energy at these frequencies is found in the PSD of the constellation red phase states; recall that the harmonic states are coupled only to the total phase state $\hat{\theta}_i(t)$, not $\hat{p}_i(t)$. Indeed, further analysis shows that 95% and 93% of the energy has been effectively removed from the red phase states in comparison to the total phase. These conclusions validate the harmonic states of the model Equation (3).

Clock Predictions

We next present the results of predicting the clock states over various intervals of interest. In order to validate the quality of the predictions, we compare each clock's predicted total phase relative to the non-predicted estimates, or zero age estimates. The prediction error is therefore defined as

$$P_i(t_k+\tau) \;=\; \mathbf{H}\Phi(\tau,t_k)\hat{\mathbf{x}}_i(t_k) - \mathbf{H}\hat{\mathbf{x}}_i(t_k+\tau), \qquad (19)$$

where $\mathbf{x}$ is the full state vector and Φ is the full transition matrix; the role of the observation matrix $\mathbf{H}$ is to simply extract the predicted total phase state.

Finally, the statistic β_i that will be calculated for each of the above prediction errors is a maximum daily RMS of the differences. To clarify this statistic, first let T be the set of all epochs from which clock predictions will be computed. Let the set of numbers

$$\{d_0, d_1, d_2, \cdots, d_n\}$$

denote the daily epochs at 00h00. Then, we partition the set of epochs T into the set decomposition

$$T \;=\; T_1 \cup T_2 \cup \cdots \cup T_n,$$

where $T_i \;=\; T \cap [\,d_{i-1}, d_i\,]$. Then,

$$\beta_i(\tau) \;:=\; \max_{1\le \ell \le n} \left\{ \operatorname*{RMS}_{t_k \in T_\ell} \{ P_i(t_k+\tau) \} \right\}.$$

The maximum daily RMS error statistic allows some averaging of error similar to an overall RMS but also captures any large day-to-day deviations that might otherwise be smoothed over longer datasets.

Prediction errors of Equation (19) were tabulated for each clock from the ETF estimates obtained and maximum daily RMS statistics $\beta_i(\tau)$ calculated for intervals of τ = 1, 3, 6, 12, and 24 hours. Table 4 summarizes the results. The very large errors for PRN11, PRN17, PRN22, PRN28, and PRN29 are attributed to anomalous clock behavior seen in these clocks over this period. Indeed, as Figure 7 shows, these clocks are exhibiting behavior that is not representative of the ETF model nor are the behaviors consistent with simple isolated phase or frequency breaks that the ETF is equipped to handle automatically. Therefore, these clocks cannot be well predicted over this period.

For other clocks having isolated but random frequency breaks such as PRN01, the ETF correctly detects and mitigates the effect of the frequency break as shown in Figure 8. The figure shows ETF filter states for SVN63/PRN01 over the 1 month period of January 2015; the total phase and phase states are plotted in black and gray, respectively, and its frequency state and drift states are plotted in red and blue, respectively, each on separate scales shown in the same color. Also included in the figure is the 1-day total phase predictions for the clock shown in purple. The very large random frequency break in mid-January is properly detected by the ETF, albeit with a lag of several days and only after

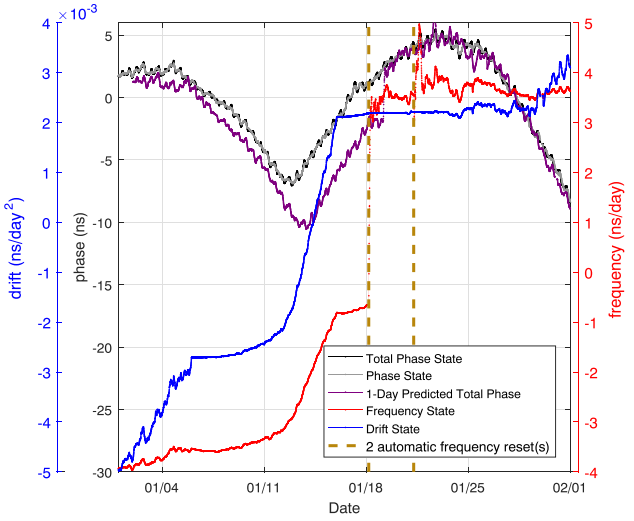

Fig. 8–ETF filter states for SVN63/PRN01 over the one-month period of January 2015, where the total phase and phase states are plotted in black and gray, respectively; frequency state plotted in red, drift state plotted in blue, each on separate scales shown in the same color. Also included is the one-day total phase predictions (purple) for the clock. The very large random frequency delta in mid-January is properly detected by the ETF (with some lag) and after two adjustments is compensated by the ETF by injecting enough noise into the frequency variance state to learn the new frequency offset. During the period of mitigation, the clock was automatically removed from the ensemble and decorrelated from other clocks. [Color figure can be viewed at wileyonlinelibrary.com and www.ion.org]

Table 4 — ETF clock prediction errors in centimeters calculated as the maximum daily RMS differences between the ETF estimates/predictions for each satellite versus the unfiltered clock data. The results were calculated over the period January 1, 2015 through March 31, 2015. These results represent the performance of the GPS constellation as of Q1 2015. Several satellite clocks during this time do not meet the OCX specification and it is expected that better stability will be realized in the OCX system.

Satellite	Block	Active Clock	Prediction Error for Interval, τ						Comment
			ZAOD (cm)	1-hour (cm)	3-hour (cm)	6-hour (cm)	12-hour (cm)	1-day (cm)	
PRN 1 Nav 63	IIF	Rb	4.2	18.9	39.3	51.5	26.3	43.6	large freq. break auto-fixed
PRN 2 Nav 61	IIR	Rb	2.6	8.9	16.2	24.3	38.3	68.3	
PRN 3 Nav 69	IIF	Rb	NaN	NaN	NaN	NaN	NaN	NaN	
PRN 4 Nav 34	IIA	Rb	3.1	27.2	66.5	112.4	126.0	305.2	four freq. deviations not fixed
PRN 5 Nav 50	IIRM	Rb	2.6	12.2	23.5	33.7	36.0	52.7	
PRN 6 Nav 67	IIF	Rb	3.2	12.7	28.8	36.1	41.2	54.2	
PRN 7 Nav 48	IIRM	Rb	2.4	10.7	22.6	33.6	53.5	97.4	
PRN 8 Nav 38	IIA	Cs	2.9	NaN	NaN	NaN	NaN	NaN	Cs clock
PRN 9 Nav 68	IIF	Rb	1.5	7.8	11.0	14.0	21.2	50.1	
PRN 10 Nav 40	IIA	Cs	1.7	70.1	140.5	194.4	311.6	534.7	Cs clock
PRN 11 Nav 46	IIR	Rb	3.0	13.7	31.4	47.1	86.6	160.5	anomalous (see Fig. 7)
PRN 12 Nav 58	IIRM	Rb	2.1	17.0	43.2	83.5	82.8	105.2	
PRN 13 Nav 43	IIR	Rb	2.3	12.6	21.5	33.5	59.5	92.4	
PRN 14 Nav 41	IIR	Rb	3.1	10.9	63.9	85.6	123.2	320.9	
PRN 15 Nav 55	IIRM	Rb	2.2	10.9	22.9	26.4	21.6	33.0	
PRN 16 Nav 56	IIR	Rb	2.8	14.5	26.6	30.0	24.0	43.1	
PRN 17 Nav 53	IIRM	Rb	2.9	28.8	77.8	168.5	363.3	731.7	anomalous (see Fig. 7)
PRN 18 Nav 54	IIR	Rb	2.5	12.6	23.2	26.1	29.7	55.3	
PRN 19 Nav 59	IIR	Rb	2.4	10.2	22.7	39.2	61.9	128.4	
PRN 20 Nav 51	IIR	Rb	2.4	10.7	19.1	32.4	65.1	130.0	
PRN 21 Nav 45	IIR	Rb	4.1	18.0	42.6	77.0	142.9	299.6	excessive freq breaks in Jan.
PRN 22 Nav 47	IIR	Rb	2.3	28.2	82.0	163.3	295.2	611.3	anomalous (see Fig. 7)
PRN 23 Nav 60	IIR	Rb	2.1	7.8	11.8	15.6	24.3	37.4	
PRN 24 Nav 65	IIF	Cs	2.1	47.5	94.3	152.1	273.8	436.7	Cs clock
PRN 25 Nav 62	IIF	Rb	1.9	7.3	14.3	17.3	15.2	26.2	
PRN 27 Nav 66	IIF	Rb	3.2	7.5	15.1	18.5	19.0	31.6	
PRN 28 Nav 44	IIR	Rb	2.6	23.1	61.1	119.7	249.1	462.7	anomalous (see Fig. 7)
PRN 29 Nav 57	IIRM	Rb	2.1	21.3	56.3	101.2	182.0	328.0	anomalous (see Fig. 7)
PRN 30 Nav 64	IIF	Rb	4.0	15.1	34.1	48.2	45.7	111.6	
PRN 31 Nav 52	IIRM	Rb	2.5	10.4	22.6	38.3	67.3	130.7	
PRN 32 Nav 23	IIA	Rb	2.5	68.3	98.9	147.8	119.3	194.9	anomalous (see Fig. 7)

two attemps. The prefit residuals are used to estimate the amount of frequency adjustment necessary and because these values are noisy, the break is fixed only after two attempts. During the period of mitigation, the clock was automatically removed from the ensemble and decorrelated from other clocks to prevent the timescale from being affected. Note also that the maxium daily RMS prediction errors for the clock remain quite small, which would not have been the case had the break gone unhandled.

Excluding the anomalously behaving satellites, four other satellites have relatively higher prediction errors than the others, SVN38/PRN08 (BIIA Cs), SVN40/PRN10 (BIIA Cs), SVN65/PRN24 (BIIF Cs), and SVN45/PRN21. We note that three of these are Cs clocks for which one expects larger errors during nominal performance. SVN45 had several large frequency breaks together in January 2015 also near the drift upload that drove the maximum daily RMS statistic; this behavior could be considered anomalous, but only during the January period. The remaining 20 satellites all showed very good prediction errors over the full test period.

CONCLUSIONS

The results in this paper demonstrate some of the primary capabilities of the NRL Ensemble Timescale Filter. It was shown that the incorporation of fixed-period harmonic states especially for the GPS satellite clocks provides a very accurate model for predicting the constellation clocks and for improving their contribution to the ensemble timescale. Even at prediction intervals of one day, many of the Block IIF Rb clocks have errors well below 100 cm, nearly all below 150 cm. Without

compensating the harmonics which have amplitudes of up to 2 ns, these small errors would not be accounted. It should be noted however that these additional harmonic states are not currently included in the GPS navigation message and so users would not necessarily be able to take full advantage of the prediction improvements without including the harmonic state/covariance information in the navigation message.

It was also shown in these results that multiple clock weighting provides the capability to better utilize classes of mixed clock types since varied levels of different noise types may be tuned separately. The timescale derived from processing the NGA test network data through the ETF showed very good stability over all averaging intervals, where no single clock carried more than about 9% of weight(s). The timescale as tuned for this time period showed frequency stabilities reaching into the upper 10^{-16} level for averaging intervals greater than 12 days.

Finally, auto-breaking, outlier rejection, and other robustness features like the pivot clock selection also show good promise for minimizing some of the more common clock problems one might encounter, such as automatically compensating phase jumps in ground station clocks whenever the clock has undergone maintenance, or for compensating random frequency breaks which can sometimes happen in the rubidium clocks. Of course, the lag associated with the detection and mitigation of frequency breaks leaves the operator with the decision to either accept the lag in favor of minimal operator intervention, or rewind the filter and insert a manual frequency adjustment in the filter to allow the clock to be brought back into the ensemble more quickly. Either way, the ensemble is protected from any anomalous behavior that doesn't fit the ETF model.

The upgrade of the GPS control segment is still an ongoing developmental effort and therefore much can and likely will evolve between the current time and the time of operational deployment. Preliminary results have shown that the modeling and other algorithm improvements made in the NRL ETF would benefit GPS operations and provide improvements to its clock prediction capabilities and overall timescale stability.

ACKNOWLEDGEMENTS

The authors would like to recognize many members of the JPL OCX Team for their collaborative efforts and support in this development.

APPENDIX: Matlab Code for Generating Maximum Likelihood Estimate

```
% MEST.  Don Percival's Maximum Likelihood estimator.
%    [RMU,S,W] = MEST(Y,A,B,MAXITS,NOM) calculates the maximum
%    likelihood estimate RMU of the values stored in Y using
%    the redescending Hampel Psi function.
%
%    A,B are optional parameters for the Hampel psi function
%    (default values are A=3.0 and B=5.5)
%
%    MAXITS is also optional and sets the maximum number of
%    iterations to employ before terminating the algorithm.
%    default value is 10.
%
%    NOM is a vector of nominal weights
%
%    S and W are both optional output values of scale and the
%    vector of weights determined for each observation.
%
%    For vectors, MEST(Y) is simply the M.L.E. of the elements.
%    For matrices, MEST(Y) is a row vector containing the M.L.E.
%    of each column.
%
%    All NaN values in Y are ignored.
%
%
%   Usage Examples:
%
%        M = MEST(x) returns the maximum likelihood estimate of the vector x.
%
%       [M,S] = MEST(x) returns the both the M.L.E. and scale
%
%       [M,S,W] = MEST(x,2,3) returns the M.L.E., the scale S, and vector of
%             weights W using A=2 and B=3 in the Hampel Psi function.
%
%   Written by:  K. Senior 18 November 2003

a = 3.0;
b = 5.5;
maxits = 10;
```

```
[nr,nc] = size(Y);

if (nargin==2 | nargin==3)
    a = varargin{1};
    b = varargin{2};
end

if (nargin==4)
    maxits = varargin{3};
end

if(nr==1 & nc>1);
    Y = Y';
    [nr,nc] = size(Y);
end

% supplemental/nominal weights
if (nargin==5)
   bwt = varargin{4};
else
   bwt = ones(size(Y));
end

% If Y is a matrix, loop over each column of Y.
R = nan(size(Y)); % preallocate
RMU = nan(nc,1);
S = [];
for n = 1:nc;
    % Only use non-NaN data
    I = find(~isnan(Y(:,n)));
    y = Y(I,n);
    bw = bwt(I);

    RMU(n) = median(y); %first guess for location parameter is median
    S(n) = median(abs(y-RMU(n))/0.6745);% first guess for scale is the MAD scale estimate

    r = ones(size(y));
    for k = 1:maxits
        it = find(y~=RMU(n));
        tmp = (y(it)-RMU(n))/S(n);
        r(it) = bw(it).*psiha(tmp, a, b)./tmp;
        r(~it) = 1;
        RMU(n) = r'*y/sum(r);
        S(n) = median(abs(y-RMU(n))/0.6745);
    end
    R(I,n) = bw.*r/sum(bw.*r); % final set of weights used.
end

if(nargout>1)
    varargout{1} = S;
end
if(nargout == 3)
    varargout{2} = R;
end

function psi = psiha(x,a,b)

% Hampel's Psi function:
%
%                    /\
%                   /  \
%                  /    \
% ______-B  -A    /      \______
%        \       /   A    B
%         \     /
%          \   /
%           \ /
psi = x;

I = find(abs(x) > a & abs(x) <= b);
psi(I) = a/(b-a)*(b*sign(x(I)) - x(I));
psi(find(abs(x)>b)) = 0;
```

REFERENCES

1. Marquis, W., and Shaw, M., "GPS III Bringing New Capabilities to the Global Community," *InsideGNSS*, Vol. 6, No. 5, 2011, pp. 34–48.
2. Senior, K. L., and Bar-Sever, Y., U.S. Naval Research Laboratory agreement to provide clock ensembling and prediction software for use in GPS OCX. *NRL Agreement 1353822* U.S. Naval Research Laboratory, 4555 Overlook Avenue S.W., Washington, D.C., September 2008.
3. Senior, K., Koppang, P., and Ray, J., "Developing an IGS Time Scale," *IEEE Transactions on Ultrasonics, Ferroelectrics, and Frequency Control*, Vol. 50, 2003, pp. 585–593.
4. Beard, R. L., and White, J. D., Common Time Reference for Naval Systems. Formal Report. *NRL/FR/8150–04–10,079* U.S. Naval Research Laboratory, 4555 Overlook Avenue S.W., Washington D.C., October 2004.
5. Senior, K., and Coleman, M. J., "Generation of Ensemble Timescales for Clocks at the Naval Research Laboratory," *Proceedings of the 46th Annual Precise Time and Time Interval Systems Applications Meeting*, Boston, MA, December 2014, pp. 98–105.
6. Jones, R. H., and Tryon, P. V., "Estimating Time from Atomic Clocks," *Journal of Research of the National Bureau of Standards*, Vol. 88, No. 1, January–February 1983, pp. 17–24.
7. Senior, K., Ray, J., and Beard, R. L., "Characterization of Periodic Variations in the GPS Satellite Clocks," *GPS Solutions*. https://doi.org/DOI:10.1007/s10291-008-0089-9, February 2008, pp. 211–225.
8. Montenbruck, O., Hugentobler, U., Dach, R., Steigenberger, P., and Hauschild, A., "Apparent Clock Variations of the Block IIF–1 (SVN62) GPS Satellite," *GPS Solutions*, Vol. 16, No. 3, July 2012, pp. 303–313.
9. Coleman, M. J., and Senior, K., "A Comparison of GPS Clock Models for the Next Generation GPS System Timescale," *Proceedings of the 43rd Annual Precise Time and Time Interval Systems and Applications Meeting*, Long Beach, CA, November 2011, pp. 501–519.
10. Grove, L. C., *Algebra*, Dover Publications, Mineola, New York, 1983.
11. Brown, R. G., and Hwang, P. Y. C., *Introduction to Random Signals and Applied Kalman Filtering*: John Wiley and Sons, New York, 3rd Edition, 1997.
12. Maybeck, P. S., *Stochastic Models, Estimation, and Control*, Vol. I (141–1), Academic Press: New York, 1979.
13. Grewal, M. S., and Andrews, A. P., *Kalman Filtering: Theory and Practice Using MATLAB,* John Wiley and Sons, New York, 4th Edition, 2015.
14. Stein, S. R., "Time Scales Demystified," *Proceedings of the 2003 IEEE International Frequency Control Symposium and PDA Exhibition Jointly with the 17th European Frequency and Time Forum*, Tampa, FL, 2003, pp. 223–227.
15. Percival, D. B., "Use of Robust Statistical Techniques in Time Scale Formation," *Proceedings of the 2nd International Time Scale Algorithm Symposium*, Boulder, Colorado, 23–25 June 1982, pp. 1–48. Report on USNO contract N70092-82-M-0579, pp. 1–48.
16. Stein, S. R., Gifford, G. A., and Breakiron, L. A., "Report on the Timescale Algorithm Test Bed at USNO," *Proceedings of the 21st Annual Precise Time and Time Interval (PTTI) Applications and Planning Meeting*, Redondo Beach, CA, 28–30 November 1989, pp. 269–288.
17. Gray, J. E., and Allan, D. W., "A Method for Estimating the Frequency Stability of an Individual Oscillator," *Proceedings of the 28th Annual Symposium on Frequency Control*, Fort Monmouth, NJ, May 1974, pp. 243–246.
18. Hutsell, S. T., "Relating the Hadamard Variance to MCS Kalman Filter Clock Estimation," *Proceedings of the 27th Annual Precise Time and Time Interval (PTTI) Applications and Planning Meeting*, San Diego, CA, 29 November – 1 December 1995, pp. 291–302.
19. Stein, S. R., "Kalman Filter Analysis of Precision Clocks with Real–Time Parameter Estimation," *Proceedings of the 43rd Annual Symposium on Frequency Control*, Denver, CO, 31 May–2 June 1989, pp. 232–236.
20. Bar-Sever, Y. E., Bertiger, W. I., Dorsey, A. R., Harvey, N. E., Lu, W., Miller, K. J., Miller, M. A., Romans, L. J., Sibthorpe, A. J., Weiss, J. P., Fernandez, M. G., and Gross, J., "*Real-Time and Post-Processed Orbit Determination and Positioning*," October 2014. US Patent 20140316697.
21. Advanced Space Position Navigation and Timing Branch, Global Positioning System Clock Analysis Quarterly Report 2015-1. *Technical Report* US Naval Research Laboratory, February 2015.
22. Advanced Space Position Navigation and Timing Branch, Global Positioning System Clock Analysis Quarterly Report 2015-2. *Technical Report* US Naval Research Laboratory, May 2015.